




 Cite this: *RSC Adv.*, 2023, **13**, 16765

# Effect of acid treatment on boosting the photoelectrochemical performance of doped and codoped $\alpha$ -Fe<sub>2</sub>O<sub>3</sub> photoanodes†

 Yujie Wang, \* Jinlong Liu, Jie Xu  and Xiaobin Hao

Acid treatment of Ti-doped  $\alpha$ -Fe<sub>2</sub>O<sub>3</sub> photoanode can reduce the onset potential and promote the photocurrent density for photoelectrochemical (PEC) water splitting reaction. However, the inner mechanism of how this occurs has not yet been clarified. This report compares the effect of HCl hydrothermal treatment on  $\alpha$ -Fe<sub>2</sub>O<sub>3</sub> photoanodes doped with Ge, Pt, Ti, and Sn or codoped with TiGe, TiPt, and TiSn. The findings show that the promotion effect of HCl hydrothermal treatment was far less significant on the Ge-, Pt-, and Sn-doped  $\alpha$ -Fe<sub>2</sub>O<sub>3</sub> than on the Ti-doped one. In contrast, the codoped photoanodes could realize a lift in the photocurrent of up to 39% at 1.23 V<sub>RHE</sub> (versus the reversible hydrogen electrode) and a reduction in the potential onset by ~60 mV after HCl hydrothermal treatment. Anatase TiO<sub>2</sub> was detected by Raman spectroscopy on the Ti-doped  $\alpha$ -Fe<sub>2</sub>O<sub>3</sub> with adequate treatment in HCl solution. Thus, the performance promotion by acid treatment was ascribed to the surface-concentrated Ti–O bonds acting as a passivation layer that could increase the charge-capture capacity and reduce the charge-transfer resistance, as demonstrated by the potential-modulated electrochemical impedance spectroscopy results. HCl treatment of the *in situ*-doped  $\alpha$ -Fe<sub>2</sub>O<sub>3</sub> and an excessive treatment time for the *ex situ*-doped  $\alpha$ -Fe<sub>2</sub>O<sub>3</sub> caused an inhibition in the PEC performance, which could be attributed to the adverse effect of lattice defects induced by acid corrosion. The application scope of HCl treatment on the doped  $\alpha$ -Fe<sub>2</sub>O<sub>3</sub> was determined by revealing its working mechanism.

Received 10th March 2023

Accepted 21st May 2023

DOI: 10.1039/d3ra01576a

[rsc.li/rsc-advances](https://rsc.li/rsc-advances)

## 1. Introduction

To meet the demand for energy structure optimization and environmental protection, photoelectrochemical (PEC) water splitting was developed as an efficient and direct way to convert solar energy to hydrogen energy.<sup>1,2</sup> The decisive factors in achieving a high solar to hydrogen efficiency for a PEC system are the photoabsorption capacity, separation efficiency of the photogenerated electrons/holes, and transfer efficiency of the photogenerated electrons/holes to water reduction/oxidation reactions on the photoelectrodes.<sup>3–5</sup> An optimal photoelectrode should meet the following requirements: (1) the conduction and valence bands should straddle the water reduction and oxidation potentials and (2) a narrow bandgap for absorbing a substantial portion of solar light.<sup>3</sup> In the choice of photoanode material for water oxidation, hematite ( $\alpha$ -Fe<sub>2</sub>O<sub>3</sub>) is regarded as one of the most promising candidates, motivated

by its broad photoabsorption scope up to 600 nm, superior stability, nontoxicity, and relatively high photon-transfer efficiency.<sup>6,7</sup> Unfortunately, besides its conduction band being lower than the water reduction potential, there are some urgent issues on the  $\alpha$ -Fe<sub>2</sub>O<sub>3</sub> photoanode that remain to be addressed, including the deactivation of photogenerated carriers by bulk recombination due to the low electron mobility and the loss of voltage input due to its sluggish water oxidation kinetics induced by severe surface states acting as surface charge-recombination centers.<sup>8–10</sup>

Doping with high-valence ions, such as Ti<sup>4+</sup>,<sup>11</sup> Sn<sup>4+</sup>,<sup>12</sup> Pt<sup>4+</sup>,<sup>13</sup> or Ge<sup>4+</sup>,<sup>14</sup> is one of the most powerful approaches for  $\alpha$ -Fe<sub>2</sub>O<sub>3</sub> modification, and has been adopted to considerably improve the electron conductivity and promote the photocurrent density of the  $\alpha$ -Fe<sub>2</sub>O<sub>3</sub> photoanode.<sup>15,16</sup> There are two conventional methods to incorporate dopants in the  $\alpha$ -Fe<sub>2</sub>O<sub>3</sub> photoanode: by adding the dopant precursor during material synthesis (*in situ* doping) or by treating with the dopant precursor before high-temperature annealing (*ex situ* doping).<sup>17,18</sup> By *in situ* doping, the dopant is distributed homogeneously in the bulk  $\alpha$ -Fe<sub>2</sub>O<sub>3</sub>. On the contrary, the dopant in the *ex situ* method is concentrated on the surface and disperses in a gradient form. Recent works have looked more into the codoping strategy with two foreign elements, which can further promote the photocurrent

School of Materials and Chemical Engineering, Chuzhou University, Chuzhou, Anhui 239000, China. E-mail: wangyj120@163.com

† Electronic supplementary information (ESI) available: *J*-*V* curves of the monodoped photoanodes before and after HCl treatment with or without H<sub>2</sub>O<sub>2</sub>.  $\eta_{inj}$ ,  $C_{trap}$ ,  $R_{ct,trap}$  curves of the monodoped photoanodes. See DOI: <https://doi.org/10.1039/d3ra01576a>



density compared with monodoping.<sup>19–23</sup> Sn and Mo codoping in  $\alpha$ -Fe<sub>2</sub>O<sub>3</sub> has realized a photocurrent density of 1.97 mA cm<sup>-2</sup> at 1.23 V *versus* the reversible hydrogen electrode ( $V_{\text{RHE}}$ ), which is much enhanced compared with Sn-Fe<sub>2</sub>O<sub>3</sub> and  $\alpha$ -Fe<sub>2</sub>O<sub>3</sub>.<sup>24</sup> Furthermore, by Pt and P codoping, Shao *et al.*<sup>20</sup> improved the photocurrent density of  $\alpha$ -Fe<sub>2</sub>O<sub>3</sub> to 2.61 mA cm<sup>-2</sup> at 1.23  $V_{\text{RHE}}$ . Unfortunately, it has been found that doping always induces a positive shift of the photocurrent onset of the  $\alpha$ -Fe<sub>2</sub>O<sub>3</sub> nanostructured photoanode. For instance, although Ti-doped  $\alpha$ -Fe<sub>2</sub>O<sub>3</sub> (Ti-Fe<sub>2</sub>O<sub>3</sub>) exhibited a remarkably higher photocurrent density than the pristine Fe<sub>2</sub>O<sub>3</sub>, there was an increase of ~100 mV in the onset potential ( $V_{\text{on}}$ ) after Pt doping.<sup>25</sup> This has been attributed to the aggregation of doping, causing excess surface states and further restricting the water oxidation kinetics.<sup>26</sup>

Efforts have been made to reduce the onset potential of the doped  $\alpha$ -Fe<sub>2</sub>O<sub>3</sub> photoanode. Besides the conventional and universal method of cocatalyst loading,<sup>27,28</sup> a surface corrosion method by acid treatment on the prepared Ti-Fe<sub>2</sub>O<sub>3</sub> was reported by Cao *et al.*,<sup>29</sup> which shifted the onset potential cathodically by about 100 mV and increased the photocurrent density by over three times at 1.0  $V_{\text{RHE}}$ . Similarly, Xiao *et al.*<sup>30</sup> enhanced the photocurrent density and lowered the onset potential by *ca.* 100 mV for the Fe<sub>2</sub>O<sub>3</sub>:Ti photoanode with HCl hydrothermal treatment. However, the working principle of acid treatment is still under debate. Cao *et al.*<sup>29</sup> proposed a back reaction suppression mechanism, but performed no underlying structural analysis. On the contrary, Xiao *et al.*<sup>30</sup> believed the induced surface defects with chemisorbed oxygen played a role in promoting the charge transfer in surface states and in suppressing the bulk charge recombination. Interestingly, both reports were focused on Ti-doped Fe<sub>2</sub>O<sub>3</sub>, although the doping method was different, being *in situ* and *ex situ* doping, respectively. It is also intriguing to determine if this acid treatment would be effective on  $\alpha$ -Fe<sub>2</sub>O<sub>3</sub> photoanodes with other dopants, such as Pt, Sn, Ge, or the associated codoped  $\alpha$ -Fe<sub>2</sub>O<sub>3</sub> photoanodes.

This work expands this enigma and systematically compares the effect of HCl hydrothermal treatment on doped  $\alpha$ -Fe<sub>2</sub>O<sub>3</sub> photoanodes with four different dopants (Ti, Sn, Pt, Ge) imported by both *in situ*- and *ex situ*-doping methods. Aiming for higher performance and a universal comparison, codoped  $\alpha$ -Fe<sub>2</sub>O<sub>3</sub> photoanodes with TiSn, TiPt, and TiGe pairs were also prepared and treated by HCl hydrothermal treatment. The effect of HCl treatment on the PEC performance was compared, and the working mechanism of HCl treatment on the performance enhancement in the Ti-doped  $\alpha$ -Fe<sub>2</sub>O<sub>3</sub> photoanodes was discussed.

## 2. Experimental details

### 2.1 Materials

Iron(III) chloride hexahydrate (FeCl<sub>3</sub>·6H<sub>2</sub>O, 99%, Greagent, Shanghai), sodium acetate (CH<sub>3</sub>COONa, 99%, Guangfu, Tianjin), hydrochloric acid (HCl, 37%, Adamas, Shanghai), titanium(IV) chloride (TiCl<sub>4</sub>, 99.6%, Alfa Aesar), chloroplatinic acid hexahydrate (H<sub>2</sub>PtCl<sub>6</sub>·6H<sub>2</sub>O, 99.9%, Adamas), tin(IV) chloride

pentahydrate (SnCl<sub>4</sub>·5H<sub>2</sub>O, 98%, Adamas, Shanghai), germanium Oxide (GeO<sub>2</sub>, 99.999%, Adamas, Shanghai), and potassium hydroxide (KOH, 90%, powder, Greagent, Shanghai) were used as received.

### 2.2 Electrodes preparation

First, the FeOOH electrodes were prepared by placing fluorine-doped tin oxide glasses (FTO, 1 × 2 cm<sup>2</sup>) in a 20 mL aqueous solution of 0.09 M FeCl<sub>3</sub>·6H<sub>2</sub>O, 0.1 M CH<sub>3</sub>COONa, and 0.23 mL HCl and hydrothermally treating at 95 °C for 135 min. Then, the FeOOH was cleaned with ultrapure water and immersed in 40 mM GeO<sub>2</sub> aqueous solution for 30 min, and then 25  $\mu$ L of 40  $\mu$ M H<sub>2</sub>PtCl<sub>6</sub> ethanol solution was added or the electrode was dip-coated with 10 mg mL<sup>-1</sup> TiCl<sub>4</sub> or 10 mg mL<sup>-1</sup> SnCl<sub>4</sub>, before calcination at 550 °C for 2 h and 750 °C for 30 min to prepare the Ti-, Sn-, Pt-, or Ge-doped  $\alpha$ -Fe<sub>2</sub>O<sub>3</sub> electrodes (labeled as Ti, Sn, Pt, or Ge). The TiGe-, TiPt-, or TiSn-codoped  $\alpha$ -Fe<sub>2</sub>O<sub>3</sub> electrodes were prepared similarly by adding Ti and the other precursor on FeOOH following the proper sequence (labeled as TiGe, TiPt, or TiSn).

### 2.3 HCl hydrothermal treatment

The above pristine, doped, and codoped  $\alpha$ -Fe<sub>2</sub>O<sub>3</sub> electrodes were hydrothermally treated in 12 mL 0.05 M HCl at 95 °C for 1 h or 2 h (labeled as H1 or H2, *e.g.*, TiGe-H1 or TiGe-H2).

### 2.4 PEC measurements

PEC tests, including linear sweep voltammetry (*I*-*V* curve), chronoamperometry (*I*-*t* curve), and electrochemical impedance spectroscopy (EIS), were performed on an electrochemical workstation (CHI 660D, Chenhua) using a three-electrode system with the  $\alpha$ -Fe<sub>2</sub>O<sub>3</sub> electrode (working area of 1 × 1 cm<sup>2</sup>) as the photoanode, a Pt net (1.5 × 1.5 cm<sup>2</sup>) as the cathode, Hg/HgO as the reference electrode, and 1.0 M KOH (pH 14.0) solution as the electrolyte. A xenon lamp (CeauLight, CEL-S500-T5) was used as the AM 1.5G simulated light emitter. The light intensity irradiated on the front side of photoanodes was 100 mW cm<sup>-2</sup>.

The bias potential *versus* RHE was calculated using the Nernst equation:

$$V_{\text{RHE}} = V_{\text{Hg/HgO}} + 0.014 + 0.0592\text{pH} \quad (1)$$

The *J*-*V* curves were scanned at a sweep rate of 20 mV s<sup>-1</sup>. The potential-simulated EIS plots were collected at frequencies ranging from 0.1 MHz to 0.1 Hz under AM 1.5G simulated light illumination with the potential ranging from -0.2 to 0.25  $V_{\text{Hg/HgO}}$ . The charge-injecting efficiencies were calculated by dividing the photocurrent density in 0.5 M H<sub>2</sub>O<sub>2</sub>-1 M KOH electrolyte by that in 1 M KOH electrolyte. The electrochemical specific surface area (ECSA) was estimated with capacitive currents from the cyclic voltammetry (CV) analysis of the electrodes with scanning rates from 20 to 120 mV s<sup>-1</sup> at an interval of 20 mV s<sup>-1</sup> using the following equation:<sup>31</sup>

$$\text{ECSA} = C_{\text{dl}}/C_s \quad (2)$$

where  $C_{dl}$  is the electrochemical double-layer capacitance and  $C_s$  is the specific capacitance of the sample per unit area, with a typical value of  $0.040 \text{ mF cm}^{-2}$ .<sup>32</sup>

## 2.5 Characterizations

Schottky field emission scanning electron microscopy (FE-SEM, SU5000, Hitachi, Japan) and scanning/transmission electron microscopy (S/TEM, FEI TalosF200S) were used for the morphology observations. Confocal Raman spectrometry (inVia™, Renishaw, UK) was used for obtaining the Raman spectra. X-Ray photoelectron spectroscopy (XPS, ESCALAB 250Xi, Thermo, USA) was used for valence state analysis. The XPS spectra calibration was done with the binding energy of the C 1s peak at 284.8 eV.

## 3. Result and discussions

As illustrated in Fig. 1a, the pristine  $\alpha\text{-Fe}_2\text{O}_3$  electrodes were prepared on FTO substrates through the traditional method, with the hydrothermally synthesized  $\beta\text{-FeOOH}$  acting as the precursor, which was converted to  $\alpha\text{-Fe}_2\text{O}_3$  after high-temperature annealing. To accomplish element doping, the Ti, Ge, Pt, or Sn precursor solution was added to the hydrothermal reaction solution or deposited on the  $\beta\text{-FeOOH}$  surface, which are recognized as the *in situ* and *ex situ* methods, respectively. Codoped  $\alpha\text{-Fe}_2\text{O}_3$  electrodes were prepared by depositing the Ti and another element precursor (Ge, Pt, and Sn) on the  $\beta\text{-FeOOH}$  surface in the appropriate sequence. Thereby, four *in situ* single-doped (labeled as  $\text{Ti}_{in}$ ,  $\text{Ge}_{in}$ ,  $\text{Pt}_{in}$  and

$\text{Sn}_{in}$ ), four *ex situ* single-doped (labeled as Ti, Ge, Pt, and Sn), and three *ex situ* codoped (TiGe, TiPt, and TiSn)  $\alpha\text{-Fe}_2\text{O}_3$  electrodes were prepared. Then all the electrodes were hydrothermally treated in 0.05 M HCl solution for 1 h (H1) or 2 h (H2). The electrodes of Ti, TiGe, TiPt and TiSn before and after HCl treatment for 1 and 2 h were observed by SEM, as shown in Fig. 1b–e. All the electrodes demonstrated a uniform nanorod structure, but the diameter varied with changing the doping elements. An exception is that an unshaped form could be seen on the TiSn sample, whereas the nanorods on the other samples showed smooth surfaces. The diameter distributions of the nanorods are shown in the insets. The average diameters of the Ti, TiGe, TiPt, and TiSn were 81.3, 56.0, 65.2, and 66.9 nm, suggesting that Ge, Pt, and Sn codoping with Ti could substantially reduce the diameter of the nanorods. Such a reduction in nanorod diameter shortens the transport distance of holes, which is in favor of reducing the recombination probability of photogenerated electrons and holes in the bulk. Moreover, HCl hydrothermal treatment barely affected the morphology or the nanorod size. Noteworthily, the unshaped form on TiSn was reduced and removed after HCl treatment for 1 and 2 h, respectively, proving that part of the materials was dissolved by acid corrosion. The ECSAs of the Ti, TiGe, TiPt, and TiSn samples were calculated by CV with varying the scanning rate, as plotted in Fig. S1.† The ECSAs of TiGe and TiSn were similar (0.56 versus 0.54), and were higher than those of Ti and TiPt (0.40 versus 0.38). This demonstrates that the ECSA was affected by the density rather than the sizes of the nanostructures. Except for the increase in the ECSA of the Ti samples, the ECSAs were barely changed by HCl treatment. The extraordinary ECSA increase for Ti may be related to nanoparticles formed by acid corrosion.

The Raman spectra of the electrodes are shown in Fig. 2. The typical symmetric vibration modes, including two  $A_{1g}$  modes at 223 and 496  $\text{cm}^{-1}$  and five  $E_g$  modes at 243, 289, 299, 407, and 609  $\text{cm}^{-1}$ , were identified, demonstrating the main structure of  $\alpha\text{-Fe}_2\text{O}_3$ . The additional forbidden vibrational mode (LO) at

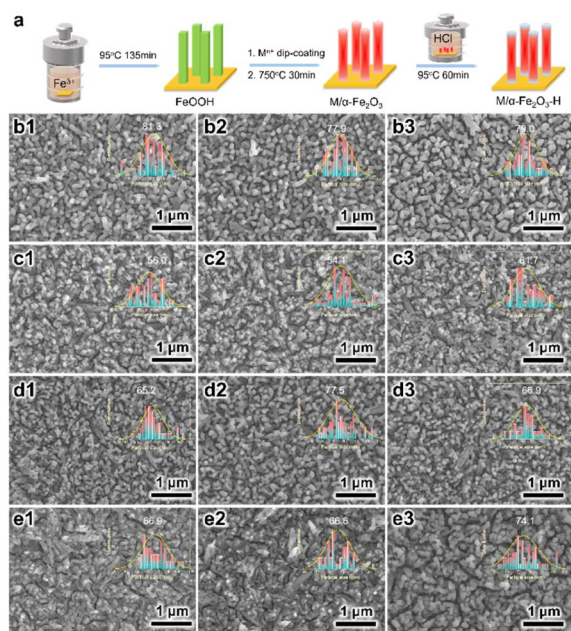


Fig. 1 (a) Preparation process of the doped ( $M/\alpha\text{-Fe}_2\text{O}_3$ ) and HCl-treated  $\alpha\text{-Fe}_2\text{O}_3$  electrodes ( $M/\alpha\text{-Fe}_2\text{O}_3\text{-H}$ ). SEM images of the (b1) Ti, (b2) Ti-H1, (b3) Ti-H2, (c1) TiGe, (c2) TiGe-H1, (c3) TiGe-H2, (d1) TiPt, (d2) TiPt-H1, (d3) TiPt-H2, (e1) TiSn, (e2) TiSn-H1, and (e3) TiSn-H2 electrodes. The size distribution curves are shown in the insets.

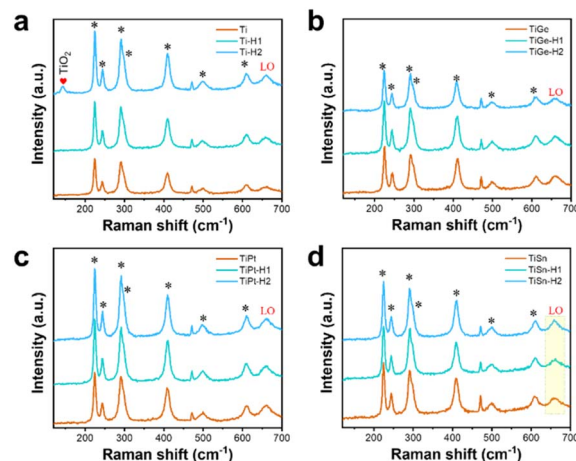


Fig. 2 Raman spectra of the (a) Ti, (b) TiGe, (c) TiPt, and (d) TiSn electrodes before and after HCl treatment for 1 and 2 h.

$\sim 660\text{ cm}^{-1}$  has been known to stem from surface structural disorders.<sup>33</sup> No change was observed in the Raman vibration peaks of  $\alpha\text{-Fe}_2\text{O}_3$  on all the electrodes with varying the doping elements or after HCl treatment, demonstrating the maintenance of the structural properties. Nevertheless, there was a significant increase in the intensity of the LO mode on TiSn compared with the other samples, as embodied by the higher intensity ratio of the LO mode *versus*  $E_g$  mode at  $609\text{ cm}^{-1}$  on TiSn. A higher LO mode corresponds to more surface disorder, coincident with the unshaped forms seen in the SEM images (Fig. 1e), implying the amorphous nature of the unshaped form induced by Sn codoping. Interestingly, a new peak at  $142\text{ cm}^{-1}$  was detected on the Ti-H2 sample, ascribed to the  $E_g$  mode of anatase  $\text{TiO}_2$ .<sup>34</sup> However, no such rise was observed on the other Ti-doped or H2 samples. The emergence of the  $\text{TiO}_2$  phase on the Ti *ex situ*-doped samples after HCl treatment for 2 h implied the phase corrosion by the acid acted on the pure  $\alpha\text{-Fe}_2\text{O}_3$  phase but with no harm to the Ti dopant. This is reasonable because  $\alpha\text{-Fe}_2\text{O}_3$  is acid dissolvable, but  $\text{TiO}_2$  is acid tolerant. Thus, it was deduced that with the continuous dissolution of  $\alpha\text{-Fe}_2\text{O}_3$  in HCl solution, the remaining Ti accumulates and forms the  $\text{TiO}_2$  phase under the hydrothermal condition. In terms of the other HCl-treated samples, the co-dopant could isolate the Ti atoms and inhibit the reconstitution of the chemical bonds.

The high-resolution XPS spectra of the electrodes are depicted in Fig. 3 and 4, and give detailed information on the elements, chemical valences, and defect states. The Fe 2p region on each sample consisted of a doublet  $2p_{3/2}$  and  $2p_{1/2}$ , topped at 710.7 and 724.3 eV, respectively, coupled with satellite peaks

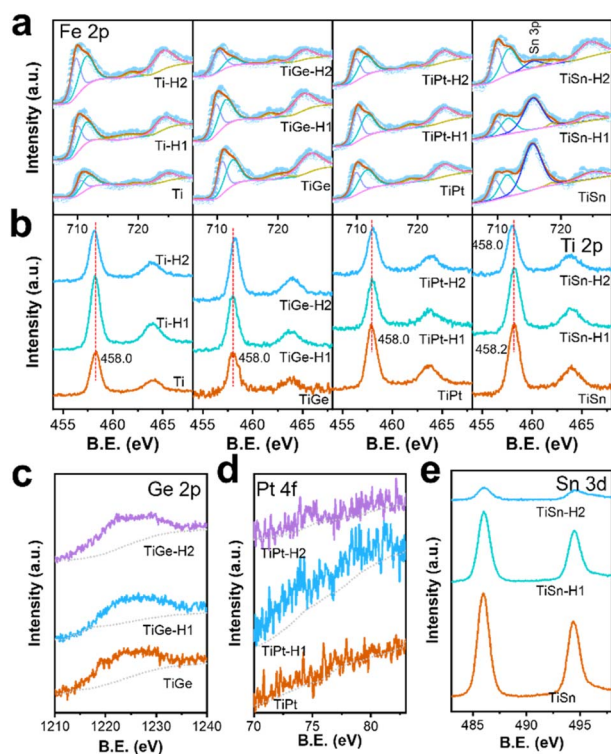


Fig. 3 XPS spectra of the (a) Fe 2p, (b) Ti 2p, (c) Ge 2p, (d) Pt 4f and (e) Sn 3d regions of the  $\alpha\text{-Fe}_2\text{O}_3$  electrodes.

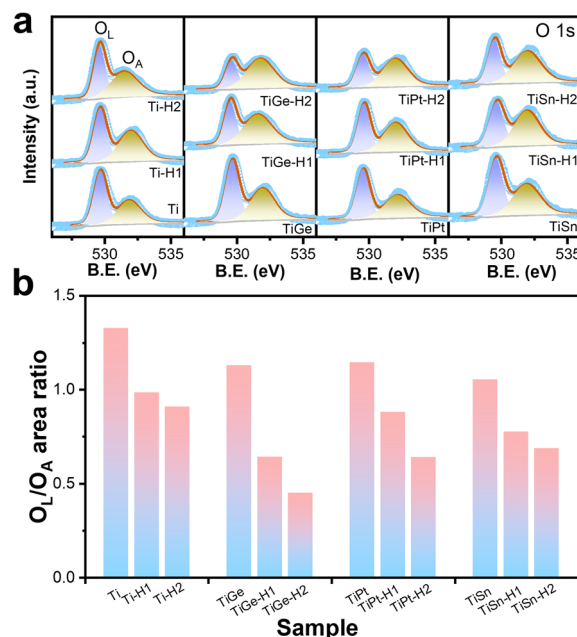


Fig. 4 XPS spectra of the (a) O 1s region and (b) the area ratios of  $O_L$  to  $O_A$  of the  $\alpha\text{-Fe}_2\text{O}_3$  electrodes.

(Fig. 3a). The satellite peak topped at  $\sim 719\text{ eV}$  was indicative of  $\text{Fe}^{3+}$ . No sign of  $\text{Fe}^{2+}$ 's existence was seen from the Fe 2p orbitals, indicating that the high-valence dopant made no difference to the electronic structure of Fe. No noticeable change in the Fe 2p spectra was seen for the Ti, TiGe, and TiPt samples before and after HCl treatment. However, a strong peak at 715.7 eV existed in the Fe 2p spectra on the TiSn samples, assigned to the Sn 3d orbital. The peak intensity of the Sn 3d orbital decreased after HCl treatment for 1 h and disappeared completely after 2 h, indicating that the Sn atoms were removed during acid dissolution. Thus, there was a discrepancy in the acid stability between the doped Ti and Sn, as the former was concentrated, but the latter was dissolved. As seen from the Ti 2p region in Fig. 3b, the Ti  $2p_{3/2}$  orbit located at 458.0 eV proved the existence of  $\text{Ti}^{4+}$ .<sup>35</sup> It was noticeable that there was a slight shift of the Ti 2p orbits to a higher binding energy on the Ti, TiGe, and TiPt samples after HCl treatment. According to the literature, the binding energy of the Ti  $2p_{3/2}$  orbit on anatase  $\text{TiO}_2$  is 459.1 eV, much higher than that of doped  $\text{Ti}^{4+}$ .<sup>34</sup> So, this further signified the concentration and reconstruction of the Ti-O bond. It was observed that the binding energy of the Ti  $2p_{3/2}$  orbit of TiSn was 458.2 eV. The higher binding energy of TiSn than Ti indicates that Sn doping affected Ti's electron structure since Sn's electronegativity was higher than that of Ti. By contrast, no shift in Ti 2p orbits was seen on the TiGe and TiPt samples, which should be related to the much lower doping amount of Ge and Pt. When TiSn was treated in HCl for 2 h, the Ti 2p orbits shifted to a lower binding energy of 458.0 eV, the same as Ti, which should be due to the removal of surface Sn. The weak Ge 2p signal topped at 1222.4 eV verified the existence of  $\text{Ge}^{4+}$  (Fig. 3c). There was only a negligible signal for Pt in the Pt 4f region in Fig. 3d because of the meager doping amount.

Fig. 3e displays the typical peaks of Sn 3d<sub>5/2</sub> at 486.0 eV and Sn 3d<sub>3/2</sub> at 496.5 eV, which are typical for Sn<sup>4+</sup>.<sup>18</sup> The peak intensity decreased significantly in the Sn 3d spectra with increasing the HCl treatment time, which was synchronous with that of Sn 3p (Fig. 3a).

As shown in Fig. 4a, the O 1s spectra consisted of two convoluted peaks centered at 529.5 and 532.2 eV, respectively, ascribed to the oxygen bonding to metal ions (lattice oxygen, O<sub>L</sub> and absorbed oxygen, O<sub>A</sub>).<sup>36</sup> The binding energies of both oxygen species were almost constant, but the relative content of O<sub>L</sub> and O<sub>A</sub> varied. The peak area ratios of O<sub>L</sub> and O<sub>A</sub> were calculated and compared in Fig. 4b. The O<sub>L</sub>/O<sub>A</sub> ratio kept going down for the Ti sample after HCl treatment, indicating HCl corrosion induced oxygen defects on the surface, consistent with the literature.<sup>30</sup> The codoped samples followed the same trend, indicating that the formation of oxygen defects by HCl corrosion was independent of the doping element.

The Ti-H2 sample was observed by TEM. A pile of nanorods with diameters ranging from 50–80 nm were observed (Fig. 5a). In the high-resolution TEM image (HRTEM, Fig. 5b), lattice spacings of 0.17 and 0.25 nm were measured, which agreed with the (116) and (110) planes of  $\alpha$ -Fe<sub>2</sub>O<sub>3</sub>. The element mapping images indicated the Ti element was dispersed on the surface of  $\alpha$ -Fe<sub>2</sub>O<sub>3</sub>, confirming the expectation that the *ex situ* method results in the aggregation of the dopant on the surface. No lattice spacing assigned to TiO<sub>2</sub> was measured. It is possible that the TiO<sub>2</sub> formed by HCl treatment existed in an amorphous phase.

The current density *versus* potential (*J*-*V*) curves of the pristine, *in situ*- and *ex situ*-doped  $\alpha$ -Fe<sub>2</sub>O<sub>3</sub> photoanodes were measured under AM 1.5G simulated light illumination. Pristine  $\alpha$ -Fe<sub>2</sub>O<sub>3</sub> exhibited a low onset potential of 0.7 V and a photocurrent density of 1.659 mA cm<sup>-2</sup> at 1.23 V<sub>RHE</sub>. By *in situ* doping with Ge, Ti, Sn, or TiSn, the onset potentials all increased, which were 0.766, 0.827, 0.806, and 0.881 V, while the photocurrent densities were 2.018, 1.874, 0.993, and 0.817 mA cm<sup>-2</sup> at 1.23

V<sub>RHE</sub>, respectively (compared in Fig. S2† and 6d). Under a certain amount of *in situ* doping, Ge and Ti enhanced the PEC performance, whereas Sn showed an adverse effect. It is more important to focus on the impact of HCl treatment on the performance of these photoanodes. As a whole, HCl treatment remarkably inhibited the photocurrent density but had little influence on the onset potential. As for the *ex situ* monodoping, the onset potentials were 0.771, 0.878, 0.878, and 0.893 V, and the photocurrent densities were 0.877, 1.430, 1.576, and 1.178 mA cm<sup>-2</sup> at 1.23 V<sub>RHE</sub> for the Ge, Pt, Sn, and Ti photoanodes, respectively (Fig. S3† and 6e). It was thus found that the *ex situ* method could induce the same (Ge doping) or higher onset potential than the *in situ* method (Ti and Sn doping). By *ex situ* codoping with TiGe, TiPt, and TiSn, there was a remarkable enhancement in PEC performance, with photocurrent densities of 1.366, 1.284, and 1.303 mA cm<sup>-2</sup> at 1.23 V<sub>RHE</sub> and onset potentials of 0.832, 0.850, and 0.897 V, respectively (Fig. 6a–c and f). It was noticed that HCl treatment lowered the onset potentials and enhanced the photocurrent density of the *ex situ*-mono- and -codoped  $\alpha$ -Fe<sub>2</sub>O<sub>3</sub> photoanodes. For example, the onset potential of Ti-H1 was 0.815 V, reduced by 78 mV, even lower than Ti<sub>in</sub>. The onset potential differences by HCl treatment of TiGe, TiPt, and TiSn were 8, 58, and 64 mV, respectively. However, the onset potential shifts of the Ge-, Pt-, and Sn-doped samples were much less significant than the Ti-doped ones. Since the *ex situ* method resulted in a gradient doping with a higher concentration on the surface while the *in situ* method formed homogeneous doping, the opposite effect in the *in situ* and *ex situ* methods by HCl treatment must be related to the dopant distribution in  $\alpha$ -Fe<sub>2</sub>O<sub>3</sub>. The transient photocurrents for Ti, TiGe, TiPt, and TiSn photoanodes were measured and are shown in Fig. S4.† At a low-bias potential of 0.84 V<sub>RHE</sub>, strong spike photocurrents were seen when the light was turned on/off. The light and dark spike photocurrents all increased after HCl treatment for 1 h and then decreased slightly after treatment for 2 h. This tendency was consistent with the *J*-*V* results. Combined with the Raman and XPS results, it could be concluded that the Ti–O bonds were concentrated on *ex situ*-Ti-doped Fe<sub>2</sub>O<sub>3</sub> after HCl treatment. It has been reported that TiO<sub>2</sub> can serve as the passivation overlayer on  $\alpha$ -Fe<sub>2</sub>O<sub>3</sub> to suppress surface electron–hole recombination.<sup>37</sup> It could thus be

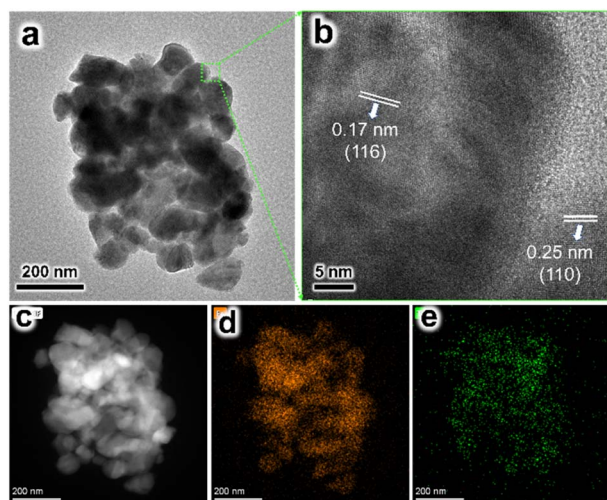


Fig. 5 (a) TEM and (b) HRTEM images of the Ti-H2 sample. (c) HAADF-STEM image of the Ti-H2 sample, and the elemental mapping images of (d) Fe and (e) Ti.

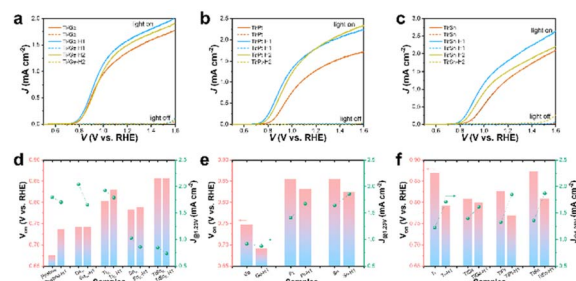


Fig. 6 Photocurrent density *versus* potential (*J*-*V*) curves of the (a) TiGe, (b) TiPt, and (c) TiSn electrodes before and after HCl treatment for 1 and 2 h. Comparison of the onset potential (*V*<sub>on</sub>) and photocurrent density at 1.23 V<sub>RHE</sub> (*J*<sub>@1.23V</sub>) of the (d) *in situ*-, (e) *ex situ*-monodoped and (f) *ex situ*-codoped  $\alpha$ -Fe<sub>2</sub>O<sub>3</sub> photoanodes.

deduced that the concentrated Ti–O on Ti *ex situ*-doped  $\alpha$ -Fe<sub>2</sub>O<sub>3</sub> was essential for reducing the onset potential. Meanwhile, Ge, Pt, and Sn barely showed such an effect.

The *J*–*V* curves of the mono- and codoped  $\alpha$ -Fe<sub>2</sub>O<sub>3</sub> photoanodes with H<sub>2</sub>O<sub>2</sub> as a hole scavenger were collected to investigate the suppressed surface charge recombination and reflect the charge-separation property. As depicted in Fig. S5a–d† and 7a–c, all the photoanodes exhibited a photocurrent density of ca. 2 mA cm<sup>−2</sup> at 1.23 V<sub>RHE</sub>, far lower than the theoretical value (12.8 mA cm<sup>−2</sup>), implying that the low charge-separation efficiency served as the major drawback for the limited PEC performance of the  $\alpha$ -Fe<sub>2</sub>O<sub>3</sub> photoanodes. The charge separation arose from ~0.5 V<sub>RHE</sub>, then increased gradually until the dark current onsets. The rate of photocurrent increase for Ge was much faster than that for the rest of the anodes, indicating smoother charge transport. Likewise, the low-bias photocurrent of TiGe was higher than that of the other codoped anodes, *e.g.*, 1.04 versus 0.45 mA cm<sup>−2</sup> at 1.0 V<sub>RHE</sub> compared with TiSn. HCl treatment for 1 h slightly improved the charge separation of all the samples, supposedly due to the surface modification's broadening of the space charge layer. Specifically, an oxidation peak appeared at 0.9 V<sub>RHE</sub> on the photocurrent and dark current of the Pt and TiPt (Figs S5b† and 7b) photoanodes, which could be assigned to the oxidation of Pt species. This implied that Pt existed as low-valence Pt instead of Pt<sup>4+</sup> on the surface. HCl treatment caused a significant decrease in the peak intensity of Pt but only a slight decrease in PtTi, giving hints that the dissolving of Pt atoms was more severe in the Pt sample than in the PtTi sample during HCl corrosion. Recalling the XPS result that Ti atoms survived during corrosion but Sn was significantly dissolved, the situation of Pt is more complicated as Ti can protect Pt from dissolving. Here,  $\eta_{inj}$  started from 0.7–0.8 V and increased steeply until reaching a plateau. The poor  $\eta_{inj}$  limited the PEC performance of the  $\alpha$ -Fe<sub>2</sub>O<sub>3</sub> photoanodes at low bias and the charge-transport efficiency at high bias. The  $\eta_{inj}$  plateaus were 82%, 58%, 82%, and 83% for the Ge, Pt, Ti, and Sn anodes, respectively. These indicate that Ti and Sn doping was much more efficient for promoting surface charge transfer than Ge and Pt, also corresponding to the PEC performance sequence.

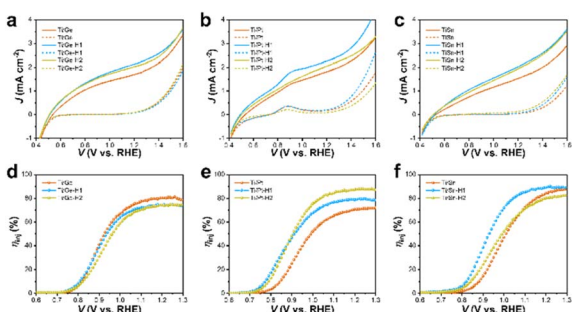


Fig. 7 Photocurrent density versus potential (*J*–*V*) curves of the (a) TiGe, (b) TiPt, and (c) TiSn photoanodes before and after HCl treatment for 1 and 2 h measured in an electrolyte with H<sub>2</sub>O<sub>2</sub> as the hole-trapping agent. Calculated charge injection efficiencies ( $\eta_{inj}$ ) of the (d) TiGe, (e) TiPt, and (f) TiSn photoanodes before and after HCl treatment for 1 and 2 h.

On the whole, the  $\eta_{inj}$  was enhanced by HCl treatment for 1 h, but then decreased after treating for 2 h (Fig. S5e–h† and 7d–f). For the codoped anodes, HCl treatment could significantly increase the  $\eta_{inj}$  plateau from 71.9% to 88.9% for TiPt, but the  $\eta_{inj}$  of TiGe was only negligibly affected by HCl treatment. For TiSn, HCl treatment increased the  $\eta_{inj}$  values between 0.8 and 1.2 V but barely affected the plateau. The effect of HCl treatment on TiPt was similar to that on Ti, but it was less significant on TiGe and TiSn, so Ge and Sn codoping inhibited the effect of HCl treatment on Ti-doped  $\alpha$ -Fe<sub>2</sub>O<sub>3</sub>. Because concentrated Ti–O accelerated the charge transfer on HCl-treated  $\alpha$ -Fe<sub>2</sub>O<sub>3</sub>, the isolation of Ti by Ge or Sn may reduce the role of HCl treatment. The changes in charge transport and injection followed the same trend due to HCl treatment, which increased first before decreasing. The changes in charge injection were much more significant, and were the main reason for the PEC performance variation.

H1 treatment essentially enhanced the  $\eta_{inj}$ , which was determined by the change in the distribution of surface states. Thereby, potential-modulated EIS measurements were conducted, and the surface capacities ( $C_{trap}$ ) and resistances ( $R_{ct,trap}$ ) related to hole trapping and transfer in the surface states were fitted according to the known equivalent circuit (Fig. S6†). The  $C_{trap}$  values represent the hole-capture capability in surface states, while the onset potential typically coincides with the location of  $C_{trap}$  maximum.<sup>38</sup> The  $C_{trap}$  plots in Fig. S7a–c† present a peak centered at 0.87–0.95 V<sub>RHE</sub> for the Ge, Ti, and Sn photoanodes, corresponding to their onset potentials with a slight shift to a higher potential. Surprisingly, the  $C_{trap}$  plots showed a steady increase within the recorded potential range for the Pt photoanode, suggesting that Pt doping significantly broadened the distribution of surface states. Considering the difference in onset potential of Pt (0.878 V) was negligible compared with that of Ti (0.891 V) or Sn (0.878 V), it could be deduced that Pt doping may induce additional surface states with a higher energy level (different kinds of surface states) instead of simply shifting the surface states to a higher energy level.<sup>9</sup> Moreover, HCl treatment shifted the surface states on Ge and Ti to a lower energy level but barely affected those on Pt and Sn, which was consistent with the change in the onset potential. The decrease in  $R_{ct,trap}$  on Ge and Ti photoanodes also indicated a smaller charge-transfer resistance facilitating charge injection, which explains the increase in photocurrent density (Fig. S7e–h†).

The changes in  $C_{trap}$  and  $R_{ct,trap}$  by HCl treatment were more significant on the codoped photoanodes, as illustrated in Fig. 8a–c. Comparably, the H1 photoanodes of TiGe, TiPt, and TiSn exhibited  $C_{trap}$  plots topped at a lower potential with larger values than the pristine ones. On the contrary, the  $C_{trap}$  values of the H2 photoanodes decreased, but the peak location stayed the same. Meanwhile, the  $R_{ct,trap}$  values below 1.0 V were remarkably decreased for the TiGe-H1 and TiPt-H1 photoanodes but the difference in  $R_{ct,trap}$  values between TiSn and TiSn-H1 was only slight (Fig. 8d–f). Besides, for each codoped photoanode, the  $R_{ct,trap}$  values of H1 and H2 were similar. This suggests the surface-concentrated Ti–O species on H1 samples contributed to shifting the surface states to a lower energy level,

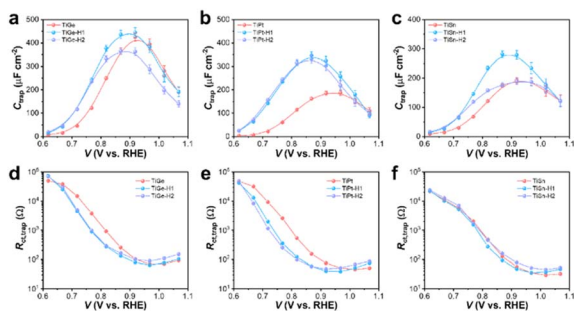


Fig. 8 Trap capacities ( $C_{\text{trap}}$ ) of the (a) TiGe, (b) TiPt, and (c) TiSn photoanodes before and after HCl treatment for 1 and 2 h. Charge-transfer resistances ( $R_{\text{ct,trap}}$ ) of the (d) TiGe, (e) TiPt, and (f) TiSn photoanodes before and after HCl treatment for 1 and 2 h.

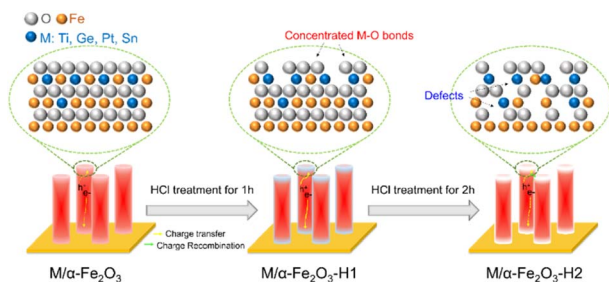


Fig. 9 Schematic of the effect of HCl treatment on Ti-doped or TiM ( $M = \text{Ge, Pt, or Sn}$ ) codoped  $\alpha\text{-Fe}_2\text{O}_3$ .

increasing the hole-trapping capacity and reducing the charge-transfer resistance. The excess lattice defects on H2 samples may be the reason for the decrease in the hole-trapping capacity, which barely affected the charge-transfer resistance. The unusual behavior of TiSn-H1, which only affected the location and density of surface states but not the charge-transfer resistance, may be related to the removal of the Sn dopant.

Based on the above discussion, the effect of HCl treatment on the Ti-, Ge-, Pt-, or Sn-doped photoanodes could be summarized, as shown in Fig. 9. The *ex situ*-doping method caused a major distribution of the dopants on the surface. Under an appropriate treatment time (1 h), part of the surface Fe-O bonds was removed, resulting in the concentration of M-O bonds, which passivated the surface states and promoted hole transfer. The promoting effect of Ti-O was the greatest among the Ti, Ge, Pt, or Sn dopants. Thus, HCl treatment contributed to a significant performance enhancement of the Ti, TiGe, TiPt, and TiSn photoanodes.

However, severe HCl treatment (2 h) further corroded the near-surface Fe-O bonds, leaving excess lattice defects that could serve as electron/hole recombination centers. Overall, HCl plays two roles in the *ex situ*-doped  $\alpha\text{-Fe}_2\text{O}_3$ : it alters the surface elemental components and forms lattice defects.

## 4. Conclusions

HCl treatment was conducted on the doped  $\alpha\text{-Fe}_2\text{O}_3$  photoanode with various dopants (Ge, Pt, Ti, and Sn) and codopants

(TiGe, TiPt, and TiSn). With the *ex situ* method used to form surface-enriched doping, an increase in photocurrent density and reduction in onset potential after HCl treatment for 1 h were realized. However, the performance enhancement was much more significant on the Ti-involved samples (Ti, TiGe, TiPt, and TiSn) than the others. The Raman spectra indicated the emergence of  $\text{TiO}_2$  species on Ti-doped  $\alpha\text{-Fe}_2\text{O}_3$ , which could act as a passivation layer to inhibit the surface charge transfer and shift the surface states to a lower energy level. It was deduced that the surface-concentrated M-O ( $M$  represents the dopant) species, especially Ti-O, improved the PEC performance. After HCl treatment for 2 h, the photocurrent density decreased, but the onset potential was unchanged. This was contributed to by the induced surface  $\text{O}_v$ , which increased as the treatment time increased. The pristine and *in situ*-doped  $\alpha\text{-Fe}_2\text{O}_3$  photoanodes (Ge, Ti, Sn, TiSn) suffered from a reduction in photocurrent density because M-O bonds could not be concentrated on the surface in the homogeneous-doped sample. This report reveals the working mechanism of HCl treatment on doped  $\alpha\text{-Fe}_2\text{O}_3$ , while also determining its application scope and providing guidance for future surface treatment study.

## Author contributions

Yujie Wang: conceptualization, investigation, methodology, writing – review & editing. Jinlong Liu: methodology, writing – original draft. Jie Xu: methodology. Xiaobin Hao: methodology.

## Conflicts of interest

There are no conflicts to declare.

## Acknowledgements

This work has been supported by the University Natural Science Research Key Project of Anhui Province (KJ2020A0707), Anhui Provincial Science and Technology Key R&D Program (2022I07020035), Key Projects of the Excellent Young Talents Support Plan in Universities of Anhui Province (gxyq2021218) and Science and Technology Project of Chuzhou (2022ZD002).

## References

- 1 A. Eftekhari, V. J. Babu and S. Ramakrishna, *Int. J. Hydrogen Energy*, 2017, **42**, 11078–11109.
- 2 H. Zhang, D. Li, W. J. Byun, X. Wang, T. J. Shin, H. Y. Jeong, H. Han, C. Li and J. S. Lee, *Nat. Commun.*, 2020, **11**, 4622.
- 3 P. Tang and J. Arbiol, *Nanoscale Horiz.*, 2019, **4**, 1256–1276.
- 4 C. Jiang, S. J. A. Moniz, A. Wang, T. Zhang and J. Tang, *Chem. Soc. Rev.*, 2017, **46**, 4645–4660.
- 5 Q. Meng, B. Zhang, L. Fan, H. Liu, M. Valvo, K. Edström, M. Cuartero, R. de Marco, G. A. Crespo and L. Sun, *Angew. Chem., Int. Ed.*, 2019, **58**, 19027–19033.
- 6 P. Wang, C. Ding, D. Li, Y. Cao, Z. Li, X. Wang, J. Shi and C. Li, *Dalton Trans.*, 2022, **51**, 9247–9255.

- 7 X. Zhao, C. Lu, S. Li, Y. Chen, G. Zhang, D. Zhang, K. Feng and J. Zhong, *J. Energy Chem.*, 2022, **69**, 414–420.
- 8 J. Xiao, H. Huang, Q. Huang, X. Li, X. Hou, L. Zhao, R. Ma, H. Chen and Y. Li, *Appl. Catal., B*, 2017, **212**, 89–96.
- 9 J. Li, W. Wan, C. A. Triana, H. Chen, Y. Zhao, C. K. Mavrokefalos and G. R. Patzke, *Nat. Commun.*, 2021, **12**, 255.
- 10 B. Du, R. Li, Y. Zhang, X. Chen, R. Tao, Z. Qin, C. Fu and J. Xiao, *Int. J. Hydrogen Energy*, 2022, **47**, 1556–1567.
- 11 J. Park, K. Y. Yoon, T. Kim, H. Jang, M. J. Kwak, J. Y. Kim and J. H. Jang, *Nano Energy*, 2020, **76**, 105089.
- 12 P. S. Shinde, A. Annamalai, J. H. Kim, S. H. Choi, J. S. Lee and J. S. Jang, *Sol. Energy Mater. Sol. Cells*, 2015, **141**, 71–79.
- 13 Y.-S. Hu, A. Kleiman-Shwarsctein, A. J. Forman, D. Hazen, J.-N. Park and E. W. McFarland, *Chem. Mater.*, 2008, **20**, 3803–3805.
- 14 K.-Y. Yoon, J. Park, M. Jung, S.-G. Ji, H. Lee, J. H. Seo, M.-J. Kwak, S. Il Seok, J. H. Lee and J.-H. Jang, *Nat. Commun.*, 2021, **12**, 4309.
- 15 C. Li, Z. Luo, T. Wang and J. Gong, *Adv. Mater.*, 2018, **30**, 1707502.
- 16 D. A. Wheeler, G. Wang, Y. Ling, Y. Li and J. Z. Zhang, *Energy Environ. Sci.*, 2012, **5**, 6682–6702.
- 17 A. Annamalai, P. S. Shinde, T. H. Jeon, H. H. Lee, H. G. Kim, W. Choi and J. S. Jang, *Sol. Energy Mater. Sol. Cells*, 2016, **144**, 247–255.
- 18 I. Kwon Jeong, M. A. Mahadik, S. Kim, H. M. Pathan, W.-S. Chae, H. Suk Chung, G. Won Kong, S. Hee Choi and J. Suk Jang, *Chem. Eng. J.*, 2020, **390**, 124504.
- 19 H. Zhang, W. Y. Noh, F. Li, J. H. Kim, H. Y. Jeong and J. S. Lee, *Adv. Funct. Mater.*, 2019, **29**, 1805737.
- 20 S. Shao, Y. Xiao, J. M. Yang, X. X. Lv, K. Feng, Y. J. Xia, D. Zhang, H. Xu, J. Zhong and J. J. Deng, *Chem. Eng. J.*, 2021, **413**, 127416.
- 21 Q. Zhu, C. Yu and X. Zhang, *J. Energy Chem.*, 2019, **35**, 30–36.
- 22 P. Huang, X. Miao, J. Wu, P. Zhang, H. Zhang, S. Bai and W. Liu, *Dalton Trans.*, 2022, **51**, 8848–8854.
- 23 S.-F. Duan, Y.-Y. Geng, X.-B. Pan, X.-Q. Yao, Y.-X. Zhao, X. Li, C.-L. Tao and D.-D. Qin, *Dalton Trans.*, 2019, **48**, 928–935.
- 24 J. Xiao, B. Du, S. Hu, J. Zhong, X. Chen, Y. Zhang, D. Cai, S.-F. Zhou and G. Zhan, *ACS Appl. Energy Mater.*, 2021, **4**, 10368–10379.
- 25 K. H. Ye, Z. L. Wang, H. B. Li, Y. F. Yuan, Y. C. Huang and W. J. Mai, *Sci. China Mater.*, 2018, **61**, 887–894.
- 26 G. Rahman and O.-S. Joo, *Mater. Chem. Phys.*, 2013, **140**, 316–322.
- 27 X. Long, P. Wang, J. Jin, X. Zhao and J. Ma, *ACS Sustainable Chem. Eng.*, 2021, **9**, 13047–13055.
- 28 D. K. Zhong and D. R. Gamelin, *J. Am. Chem. Soc.*, 2010, **132**, 4202–4207.
- 29 D. Cao, W. Luo, J. Feng, X. Zhao, Z. Li and Z. Zou, *Energy Environ. Sci.*, 2014, **7**, 752–759.
- 30 J. Xiao, F. Zhao, J. Zhong, Z. Huang, L. Fan, L. Peng, S.-F. Zhou and G. Zhan, *Chem. Eng. J.*, 2020, **402**, 126163.
- 31 R. Chong, G. Wang, Y. Du, Y. Jia, X. Wang, C. Li, Z. Chang and L. Zhang, *Chem. Eng. J.*, 2019, **366**, 523–530.
- 32 C. C. L. McCrory, S. Jung, J. C. Peters and T. F. Jaramillo, *J. Am. Chem. Soc.*, 2013, **135**, 16977–16987.
- 33 C. H. Liu, Y. Xu, H. Luo, W. C. Wang, Q. Liang and Z. D. Chen, *Chem. Eng. J.*, 2019, **363**, 23–32.
- 34 J. Liu, M. Dai, J. Wu, Y. Hu, Q. Zhang, J. Cui, Y. Wang, H. H. Tan and Y. Wu, *Sci. Bull.*, 2018, **63**, 194–202.
- 35 S. Farhoosh, B. Eftekharinia, M. Tayebi, B.-K. Lee and N. Naseri, *Appl. Surf. Sci.*, 2021, **550**, 149374.
- 36 J. Xiao, L. Fan, F. Zhao, Z. Huang, S.-F. Zhou and G. Zhan, *J. Catal.*, 2020, **381**, 139–149.
- 37 M. G. Ahmed, I. E. Kretschmer, T. A. Kandiel, A. Y. Ahmed, F. A. Rashwan and D. W. Bahnemann, *ACS Appl. Mater. Interfaces*, 2015, **7**, 24053–24062.
- 38 L. Steier, I. Herraiz-Cardona, S. Gimenez, F. Fabregat-Santiago, J. Bisquert, S. D. Tilley and M. Grätzel, *Adv. Funct. Mater.*, 2014, **24**, 7681–7688.